Journal of Fluids and Structures (1998) **12,** 295–314

EXPERIMENTAL INVESTIGATION OF A PARALLEL VORTEX–PLATE INTERACTION

J. M. Chen and C.-C. Chiou

Department of Mechanical Engineering, National Chung Hsing University, Taichung, Taiwan

(Received 26 November 1996 and in revised form 18 December 1997)

The interaction of a spanwise vortex with a flat plate was investigated experimentally in a wind tunnel. The vortex was produced by a vortex generator airfoil pitching in a tailored non-sinusoidal schedule. The smoke-wire visualization technique and unsteady surface pressure measurements were used to examine the interaction for plates having different leading-edge configurations. The results focus on transient variations of the flow structure and pressure distribution over the plate with the vortex position during the interaction. In comparison with the sharp and elliptical leading-edge plates, it was found that the passage of the vortex has a much stronger effect on the amplitude of unsteady loading for the plate with a square leading edge, primarily due to the deformation of the leading-edge separation bubble. For the examined range of vertical separation distance between the incident vortex and the test plate, it was also found that the amplitude of plate lift variation during the interaction decreases approximately linearly with the separation distance.

1. INTRODUCTION

In recent years, the interaction between vortices and structures has received increasing attention, both as a practical problem in engineering applications and a fundamental one in fluid mechanics as well. Disturbances of the flow field around the downstream structure due to incoming vortices appear to result in a generation of noise and vibrations. The phenomenon of vortex–structure interaction in real flows is a highly complex problem because it is generally three-dimensional and unsteady in nature. A large number of investigations have been conducted on the representative cases of two-dimensional (parallel) but unsteady interaction that occurs when the axis of the approaching vortex is parallel to the span of a two-dimensional structure. The interaction of a spanwise vortex with a long flat plate is one of such cases and is of interest in the present study.

A flat plate serves as a fundamental geometry of a lifting surface and as a prototype for many heat exchanger surfaces. The fluctuating loading on the plate due to an encounter with a vortex is a major concern in the area of flow-induced vibrations. Many previous studies have been made on the interactions between coherent vortices and short plates with different leading-edge configurations. Most of these studies were focused on the flow structure and fluctuating forces in the neighborhood of the leading edge. Ziada & Rockwell (1982) examined the interaction of a row of vortices in the mixing layer with the leading edge of a wedge. Their experiments were concentrated on distortion of the incident vortex during the interaction and vortex-induced secondary vortex shedding from the tip of the wedge. They found the formation of secondary vortices for some range of vertical offset between the vortex center and the leading edge. Kaykayoglu & Rockwell (1985) further measured the unsteady surface pressure on the sharp edges during the vortex-wedge interaction. The flow

0889-9746/98/030295 + 20 $25.00/fl970141

field as well as the formation and shedding of the secondary vortex during the vortex–wedge interaction were recently explored in detail by Park & Lee (1994) and Kaya & Kaykayoglu (1996) using numerical simulations. The interaction of a Karman vortex street with an elliptical leading edge was studied experimentally by Gursul & Rockwell (1990). They demonstrated and classified the different types of vortex–leading-edge interaction. Swirydczuk *et al.* (1993), in an experimental investigation of a larger edge break up (LEBU), measured the velocity fields over short plates during their interaction with incoming vortices generated by sinusoidally pitching an upstream symmetric airfoil. Their results indicated shorter plates with sharp edges to be more efficient in breaking incoming vortical structures. In addition to the plate dimension and leading-edge shape, in fact the nature of vortex–plate interaction is prevalently affected by the scale and circulation as well as relative location of the incident vortical structure with respect to the plate (Gursul & Rockwell 1990). However, the discrete vortices produced in the ways employed by the aforementioned experiments are often too close to detect the effects of an individual vortex on a flat plate which is long enough to permit measuring the chordwise pressure distribution.

There are a number of experiments related to the present study but with geometries of airfoil profiles. Seath *et al.* (1989) and Straus *et al.* (1990) investigated the blade–vortex interaction by the use of an impulsively pitching wing which created a starting vortex to interact with a downstream stationary airfoil. Their pressure measurements indicated a distinct variation of the surface pressure near the leading edge during the passage of the vortex. Straus *et al.* (1990) also reported this variation in terms of aerodynamic force and moment coefficients determined from the pressure measurements. More complete investigations of transient pressure distributions and aerodynamic loading were taken by Booth (1990) and Chen & Chang (1997), in which the incoming vortex was produced by an upstream airfoil pitching in a tailored nonsinusoidal schedule. These investigations lead to a common conclusion that the influence of the incoming vortex on the amplitude of airfoil transient loading is enhanced by an increase in the incidence of the downstream test airfoil and a reduction of the vertical offset of the vortex generator. The wakes generated by a nonsinusoidally oscillating airfoil and their interactions with a downstream stationary airfoil were recently simulated by Mook & Dong (1994) with the vorticity-panel method.

The present experimental investigation aims to reveal the unsteady features of the interaction between a spanwise vortex and a long flat plate. Differing from previous studies of vortex–edge interactions, the emphasis of the present experiments is placed on transient changes of the flow structure and pressure distribution over the plate during the interaction. One of the main difficulties arising in the experiments was the generation of a well-defined vortex. The vortex generation technique adopted here was similar to the one used by Booth (1990) and Chen & Chang (1997), which provided good repeatability and favorable accuracy of measurements. The smoke-wire technique was utilized for the present investigation to exhibit the variation of the flow structure. Phase-averaged surface pressure measurements were carried out to explore the quantitative response of the test plate to the passage of the vortex. The pressure distributions were further integrated to obtain the unsteady loading on the plate. Plates having different leading-edge configurations were examined for the present experiments. Furthermore, the vertical offset of the vortex generator was varied in the experiments, to allow the center of the incident vortex to collide head-on with the test plate or to pass aside from the plate.

2. EXPERIMENTAL SETUP

The experiments were conducted in an open-type wind tunnel with a square test-section of 305 mm × 305 mm and 1100 mm long. The flow into the test-section had a turbulence level less than 0·5% for the velocity range tested in the present experiments. Three types of long flat plates having square, sharp and elliptical leading edges, as shown in Figure 1, were used for the test models. All plates which were made of plexiglass had a thickness $H = 6$ mm and a chord $C = 120$ mm. The chord-to-thickness ratio is large enough for the interaction between separated shear layers on both sides of the plate to be negligible. The test-plate was horizontally mounted between the side plates of the test-section, giving a span-to-thickness ratio of 50·8. This large span-to-thickness ratio helps to minimize three-dimensional effects in the central portion of the test-section.

The incident vortex was produced by a vortex generator consisting of a 50 mm chord NACA 0015 airfoil located upstream of the test-plate. Figure 2 illustrates the geometric parameters of the experimental arrangement. The vertical offset of the vortex generator, Y_v, with respect to the test-plate could be adjusted for each experiment. The vortex generator

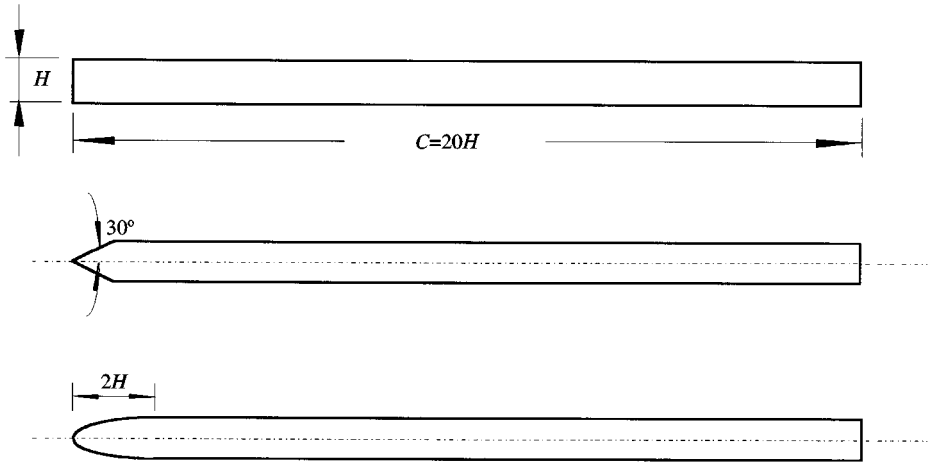

Figure 1. Three types of flat plates tested in the experiments.

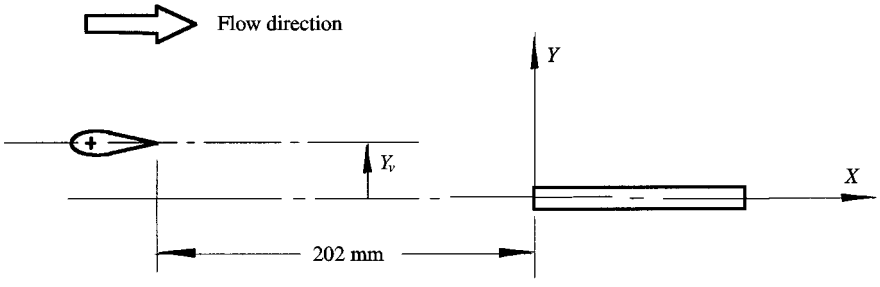

Figure 2. Geometric parameters of the experiments.

that spanned the test-section was driven by a digital control servomotor about its quarter chord. An optical encoder coupled to the motor shaft enabled to signify the transient angle of incidence of the vortex generator to an accuracy of 0·09°. The signal from the encoder was used as the phase reference for flow visualization and pressure measurements. In order to create a well-defined, relatively isolated vortex, the vortex generator was oscillated in a tailored nonsinusoidal schedule, i.e. a sinusoidal pitch-up stroke from 12 to $-12°$ in 80 ms was followed by a constant-rate pitch-down stroke from 12 to $-12°$ in 200 ms. The actual pitch schedule of the vortex generator is illustrated in Figure 3. A relatively isolated region of concentrated vorticity could be created during the rapid pitch-up stroke, while the vorticity generated during the slow pitch-down stroke was much weaker (Mook & Dong 1994). The repeatability of the vortex generator motion is critical to the present experiments. Repeat tests showed that the variation between pitching cycles of the vortex generator was not more than 0·25°.

The smoke-wire technique was employed to visualize the unsteady flowfield during the interaction of the incident vortex with the test-plate. A corrugated nichrome wire of 100 μm diameter was placed vertically in the centerplane of the test section at 40 mm downstream the vortex generator. Kerosene was drip-coated on the wire from an oil cup. To generate smoke streaks the wire was heated at a voltage of 20–30 V. The visualized flow field was illuminated by a laser sheet provided with a light source of a 5 W laser (Coherent Innova 90). The flow structure was recorded by an image acquisition and processing system consisting of a frame grabber (Coreco Oculus-F/64), a CCD camera, and a personal computer. This image processing system could be triggered to take sequential photographs by a pulse at a particular time that was phase-referenced to the instantaneous angular position of the vortex generator.

Response of the test-plate to the passage of incident vortex was explored using pressure measurements on the plate surfaces. A total of 28 pressure ports were located on the upper and lower surfaces along the mid-span of the plate at $X = 5$, 10, 15, 20, 30, 40, 50, 60, 70, 80, 90, 100, 110 and 115 mm. Two additional ports were positioned at ± 60 mm from the

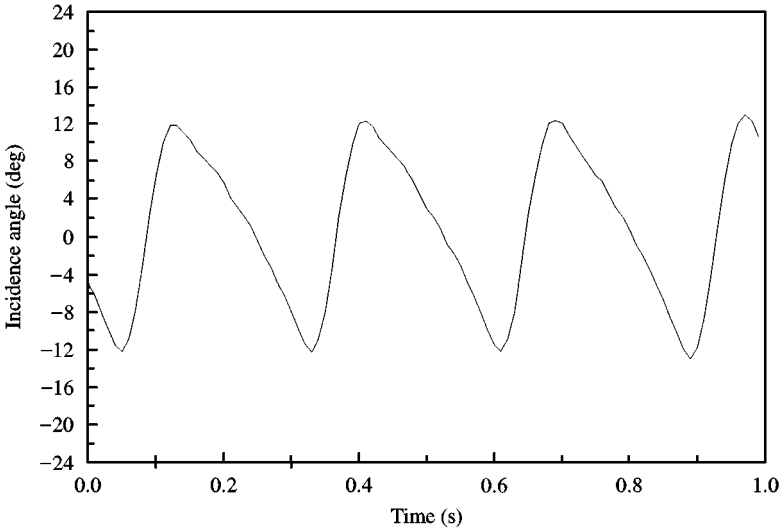

Figure 3. Actual time history of the angular position of the vortex generator.

mid-span, at $X = 30$ mm, to check for three-dimensional effects. This chordwise location was chosen for the reason that pressure variations were relatively more pronounced in the forward 25% chord length for most of the interactions considered. The maximum variation of the pressure coefficient C_p between the three different spanwise locations was found to be small (within $\pm 4.5\%$). The diameter of each pressure port was 0·6 mm. The unsteady surface pressures were measured using Setra 239 differential pressure transducers connected to the pressure ports with short tubes of equal length. The natural frequency of the transducer was higher than 1 kHz. Although the connection of the tubing to the transducer could considerably reduce the overall dynamic response, such an arrangement for pressure measurements sufficed for the dynamic range of interest in the present investigation.

The measurements of pressure were recorded by a multi-channel analog data acquisition memory (ADAM ADC0512) which had an individual A/D converter on each channel. The ADAM system was used mainly for recording and displaying of sudden and transient signals. In order to obtain the unsteady mean pressure distribution, the ensemble averaging was employed with six oscillation cycles at each pressure port. This number of ensembles was a compromise between overall measurement time and accuracy. The estimated uncertainty (due to random errors) of the pressure coefficient C_p was less than 3% of the maximum value. The solid blockage due to the test-plate was 2%. No corrections were made on the pressure measurements for blockage effects. Moreover, to confirm that the test plate was at zero incidence to the freestream, before each of the experiments, time-averaged pressures at equivalent chordwise positions on the upper and lower surfaces were usually found to agree within 0·01 in C_p.

Flow visualization and pressure measurements were performed at the same freestream velocity $U = 2{\cdot}5$ m/s, corresponding to a Reynolds number of 20 000 based on the plate chord.

3. RESULTS AND DISCUSSION

3.1. Quasi-Steady Flow over Flat Plate

To serve as a basis for comparison with the results of the unsteady experiments, the surface pressure measurements were first made on the flat plate encountering a smooth flow. The time-averaged pressure distributions of the three different plates are shown in Figure 4. For the square leading-edge plate, the distribution begins with a flat plateau region of low pressure, immediately downstream of the leading edge. Subsequently, the pressure increases sharply to reach a higher level of C_p with a small pressure gradient beyond $X/C = 0{\cdot}34$. It has long been recognized that the flow past a blunt flat plate is characterized by a separation bubble formed along the plate just behind the leading edge and reattachment of the separated shear layer to the downstream plate surface (Ota & Itasaka 1976; Cherry *et al.* 1984). Therefore, the low pressure plateau observed in Figure 4 responds to the separation bubble, and the averaged reattachment point occurs near $X/C = 0{\cdot}25$, a position slightly upstream of the maximum pressure (Kiya & Sasaki 1983*a*). Moreover, the small pressure gradient in the downstream position may be attributed to flow redevelopment in the boundary layer beyond the reattachment (Ota & Itasaka 1976). For the sharp and elliptical plates, the low-pressure plateau is not observed; instead, relatively smaller variations occur in the leading 17% of the chord as a reflection of their edge geometries. Thereafter, the pressure maintains a nearly constant value until $X/C = 0{\cdot}8$, signifying attached laminar flow in the downstream boundary layer. Note that, after $X/C > 0{\cdot}8$, the distribution shows

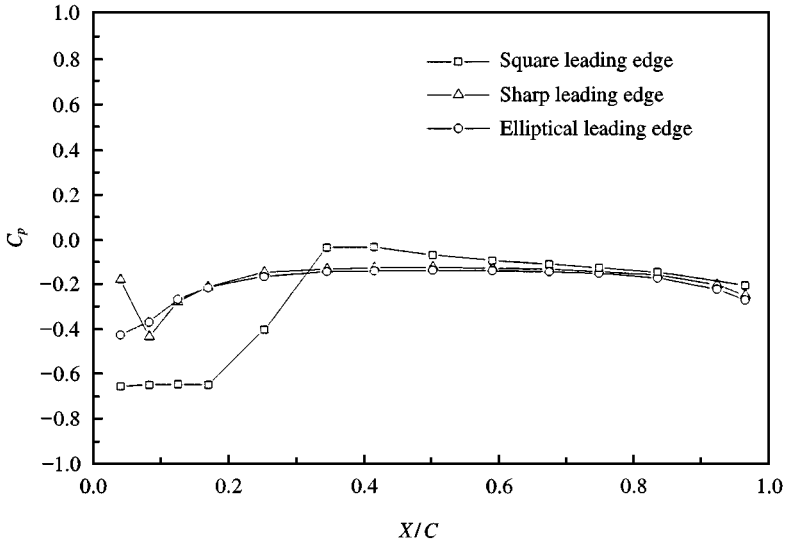

Figure 4. Comparison of the time-averaged pressure distributions on the upper surface for quasi-steady flow past the three types of plates: □, square leading edge; △, sharp leading edge; ○, elliptical leading edge.

a gradient toward negative C_p values due to the effect of the wake. It was observed in smoke visualization that the wake of the sharp and elliptical plates consisted of well-organized discrete vortices formed immediately behind the trailing edge.

3.2. Generation of Single Vortex

The incident vortex was generated from the roll-up of the vortex wake that was shed from the vortex generator airfoil during a rapidly pitching motion. The mechanism concerning the incident vortex generated by such a means has been discussed in some detail in the numerical simulations of Mook & Dong (1994) and in a visualization study of the flow field by Chen & Shieh (1997). Figure 5 shows the development of the incident vortex. The wake preceding the shedding of the well-defined incident vortex is depicted in Figure 5(a). When the vortex generator rapidly pitches up from $\alpha = -12^\circ$, the counter-clockwise vorticity is accumulated in the vicinity of the trailing edge to form a well-defined vortex. This vortex is shed from the trailing edge and convects downstream. The convection and development of the vortex are portrayed in Figure 5(b–d) for the streamwise locations of the vortex at about $X_v/C = -0{\cdot}6$, 0 and 0·6, respectively. Note that this well-defined incident vortex is accompanied by vortices of smaller scale created during the slow pitch-down stroke from $\alpha = 12^\circ$ to -12°. The separation distance between consecutive incident vortices is on the order of five plate chord lengths. The influence of the smaller vortices on pressure measurements on the plate downstream may be negligible after the phase averaging. It was found that the averaged peak-to-peak amplitude of the fluctuation in C_p on the first top pressure port of the plate due to the smaller vortices occurred between 0·03 and 0·06 which was less than 5% of the variation induced by the incident vortex. After comparing a series of flow visualization photographs, the incident vortex was found to maintain nearly a straight line moving downstream at a convection velocity of approximately 80% of the freestream velocity.

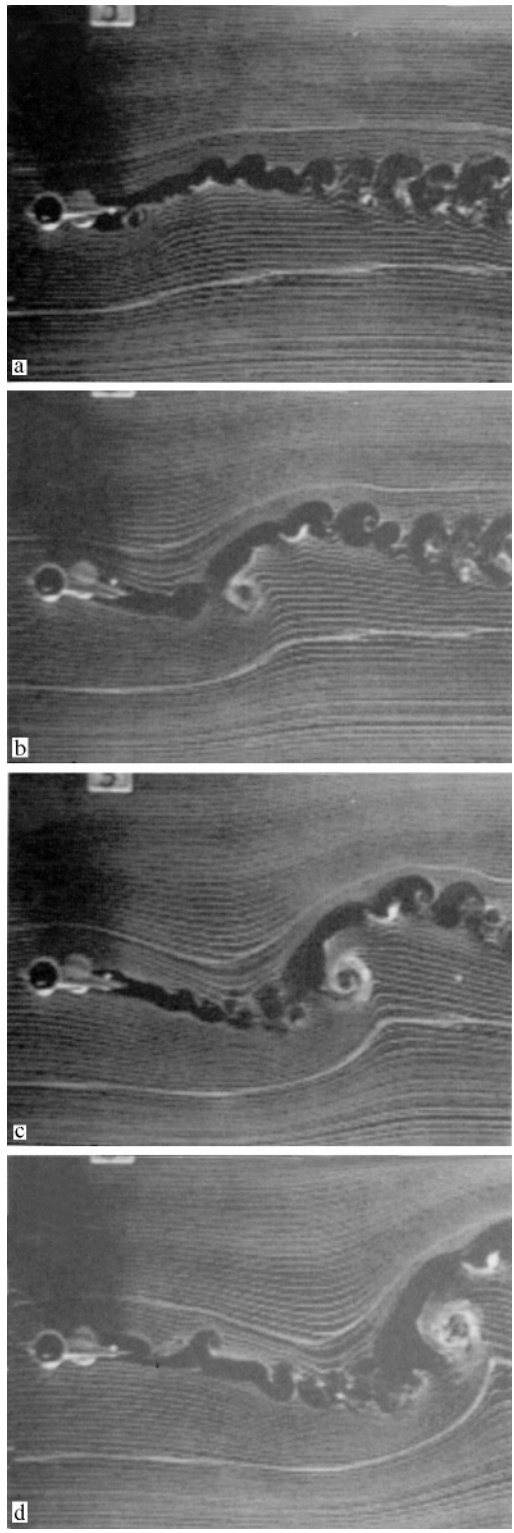

Figure 5. Smoke visualization of the development of a well-defined vortex: (a) wake before the shedding of the incident vortex; (b) $X_v/C = -0{\cdot}6$; (c) $X_v/C = 0$; (d) $X_v/C = 0{\cdot}6$.

Prior to the experiments of the interaction between the incident vortex and the downstream plate, quantitative properties of the vortex were carefully examined. The wake survey across the flow was made in the absence of the test-plate at $X/C = 0$, in which the velocity disturbances induced by the vortex were embedded in the flow. The diameter of the vortex core is taken as the distance between the points at which the extremum fluctuation values of the vortex-induced velocity appear (Swirydczuk 1990). Then, by assuming the incident vortex as a type of potential vortex (Lugt 1983), the vortex is estimated to have a circulation $\Gamma = 410\,\mathrm{cm}^2/\mathrm{s}$ with a core of diameter $0{\cdot}2C$ at the plate leading edge ($X/C = 0$). The velocity fluctuations induced by the vortex as well as the vortex core boundary were discussed in detail in a paper by Chen & Shieh (1997).

3.3. Vortex-plate Interaction

The interaction of the incident vortex with the plates of different leading-edge shape has been examined for the dimensionless vertical offset in the range $Y_v/C = -0{\cdot}375$ to $0{\cdot}375$. Figure 6 shows a series of visualization photographs for a typical head-on interaction ($Y_v/C = 0{\cdot}0$) of the incident vortex with the square leading-edge plate. As the vortex

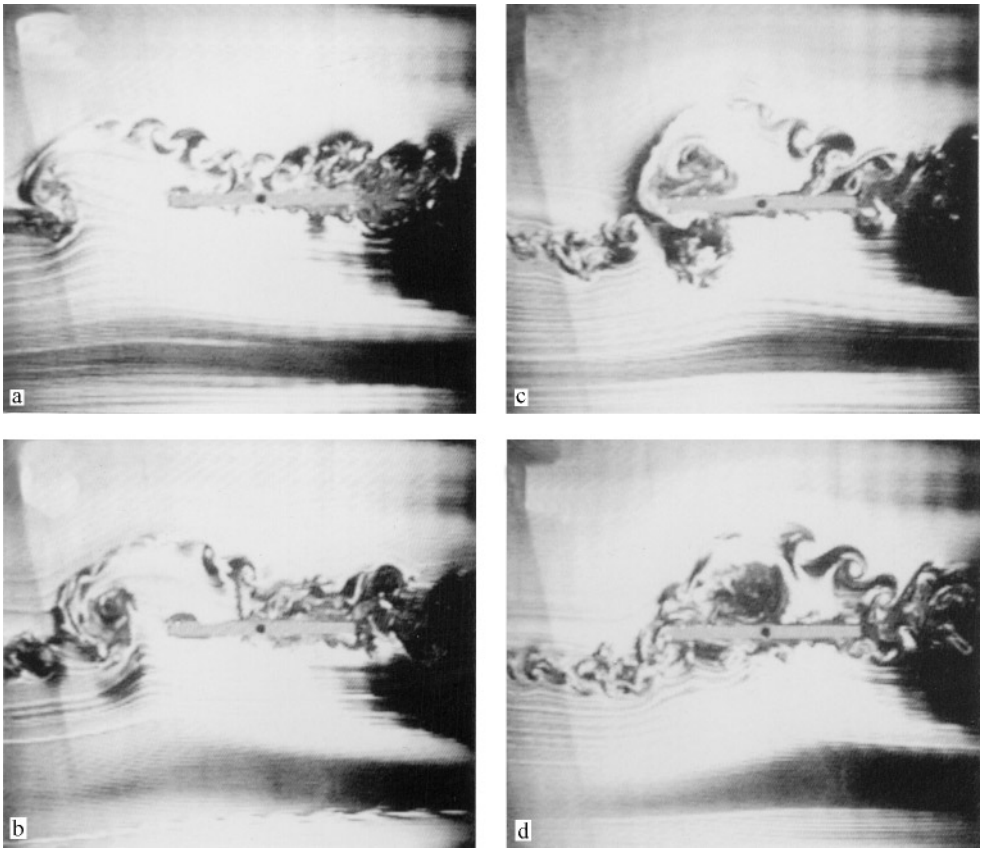

Figure 6. Smoke visualization of the interaction of the vortex with the square leading-edge plate at $Y_v/C = 0$. Time intervals relative to (a) are: (b) 0·017 s; (c) 0·050 s; (d) 0·067 s.

approaches the plate at $X_v/C = -0{\cdot}7$, it is observed in Figure 6(a) that its counter-clockwise circulation begins to influence the flow in the vicinity of the leading edge. The vortex tends to increase the local angle of attack by an upwash effect. As a result, the region of separated and reattaching flow (hereafter referred to as the "separation bubble") formed above the plate increases in thickness, while the bubble below the plate is depressed. When the vortex convects downstream close to the leading edge, Figure 6(b) shows that the separation bubble on the upper surface is enlarged, indicating further enhancement of the local upwash effect near the leading edge. When the vortex collides with the plate, the incident vortex is split into two parts, as seen in Figure 6(c). Movement of the split-incident vortex in the downstream direction seems to be affected by the separation bubbles, causing the upper portion of the split vortex to move ahead of the lower one [Figure 6(d)]. However, the separation bubble itself does not move downstream with the split vortex.

Visualization of the interaction of the vortex with the square leading-edge plate at $Y_v/C = 0{\cdot}25$ is depicted in Figure 7. It can be seen in Figure 7(a) that, due to the offset of the vortex generator, smaller scale vortices produced during the slow pitch-down stroke pass above the plate. These smaller vortices appear to have no discernible effect on the flow in the neighborhood of the leading edge, resulting in symmetric separated shear layers along the plate. As the incident vortex approaches less than a chord length from the leading edge, Figure 7(b, c) shows that the plate experiences an increase in the angle of attack by an upwash effect, and the separated shear layers are no longer symmetric. With an increase in vortex-induced upwash, the separation bubble on the upper surface increases in thickness, while it decreases on the lower surface. This indicates the build-up of a clockwise "bound" circulation around the plate whose orientation is opposite to that of the incident vortex. As the incident vortex moves close to the leading edge, Figure 7(d) shows that the vortex-induced bound circulation further increases in strength, leading to a shift of the stagnation point to the lower surface. It is also observed in Figure 7(d) that the separation bubble on the upper surface develops to a much larger size than that on the lower surface. As the incident vortex passes above the plate, the vortex preserves itself (without splitting) but is deflected upward due to the separated shear layer formed on the upper surface [Figure 7(e)]. Once the incident vortex convects over the plate midchord, it is evident in Figure 7(f) that the angle of attack changes sign due to a downwash effect induced near the leading edge, displaying a larger separation bubble on the lower surface than that on the upper surface.

Figure 8 shows the time variation of the pressure distributions on the upper and lower surfaces of the square leading-edge plate during the interaction with the incident vortex at $Y_v/C = 0$. The flow visualization depicted in Figure 6(a–d) corresponds to the time period 0·180–0·247 s in Figure 8. As the incident vortex approaches the leading edge, its counter-clockwise circulation tends to increase the local angle of attack by an upwash effect. The vortex-induced upwash causes a decrease in the upper surface pressure in the vicinity of the leading edge and an increase in the lower surface pressure. When the vortex arrives at the leading edge at time 0·22 s, there occurs the minimum pressure on the upper surface and a rapid pressure rise begins. The characteristic time of this rapid rise is about $0{\cdot}5C$ of travel. At the same time, the pressure near the leading edge on the lower surface reaches the maximum. Downstream from the leading edge, the pressure reduces drastically. As the vortex convects beyond the mid-chord (after a time of 0·25 s), the pressure progressively resumes an assumed quasi-steady case. Figure 8 also reflects pressure fluctuations due to the unsteadiness of the wake produced by the upstream vortex generator during the slow pitch-down stroke. These fluctuations are of smaller magnitude than the disturbance of the impinging vortex. It can be observed that during the time period 0·18–0·20 s, the pressure

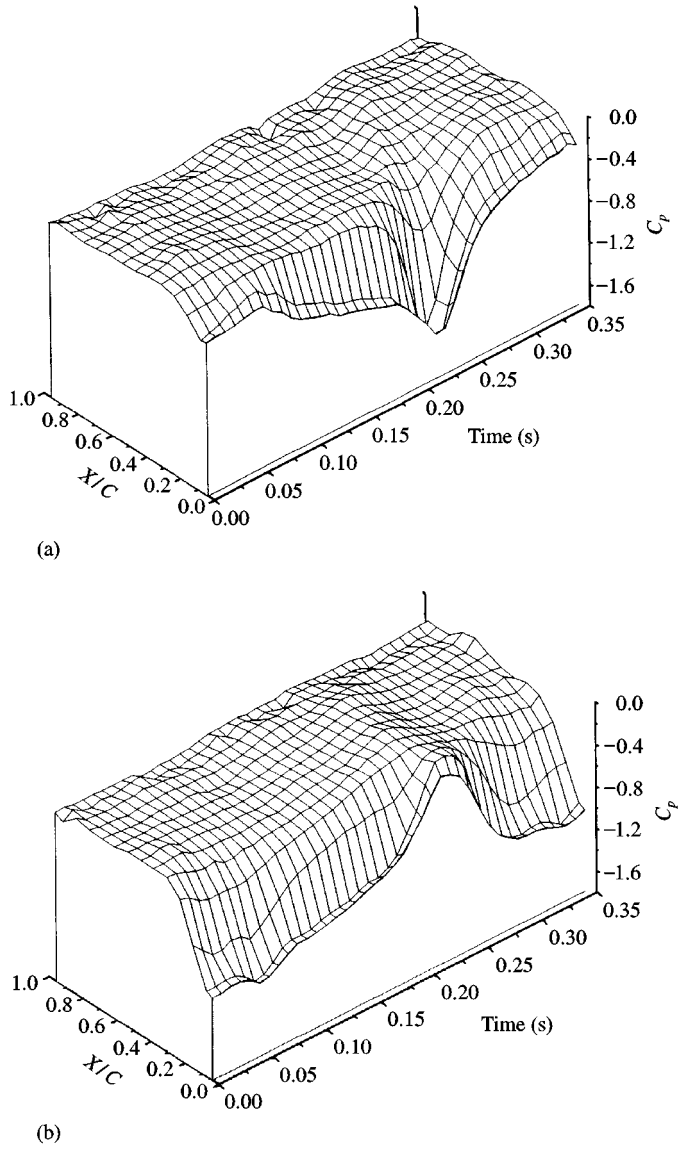

Figure 8. Time variation of pressure distributions on the square leading-edge plate at $Y_v/C = 0$: (a) upper surface; (b) lower surface.

fluctuation generated by the smaller vortices that appear above the downstream of the quarter chord ($X/C = 0{\cdot}25$–$1{\cdot}0$) in Figure 6(a, b) is weak (less than 5%), in comparison with the variation induced by the incident vortex occurring in the forward 17% of the chord.

Observation of Figure 8 indicates that the tailored pitching oscillation of the vortex generator creates a distinct alteration in the plate pressure distribution during the vortex–plate interaction. The vortex-induced alteration is most appreciable in the leading

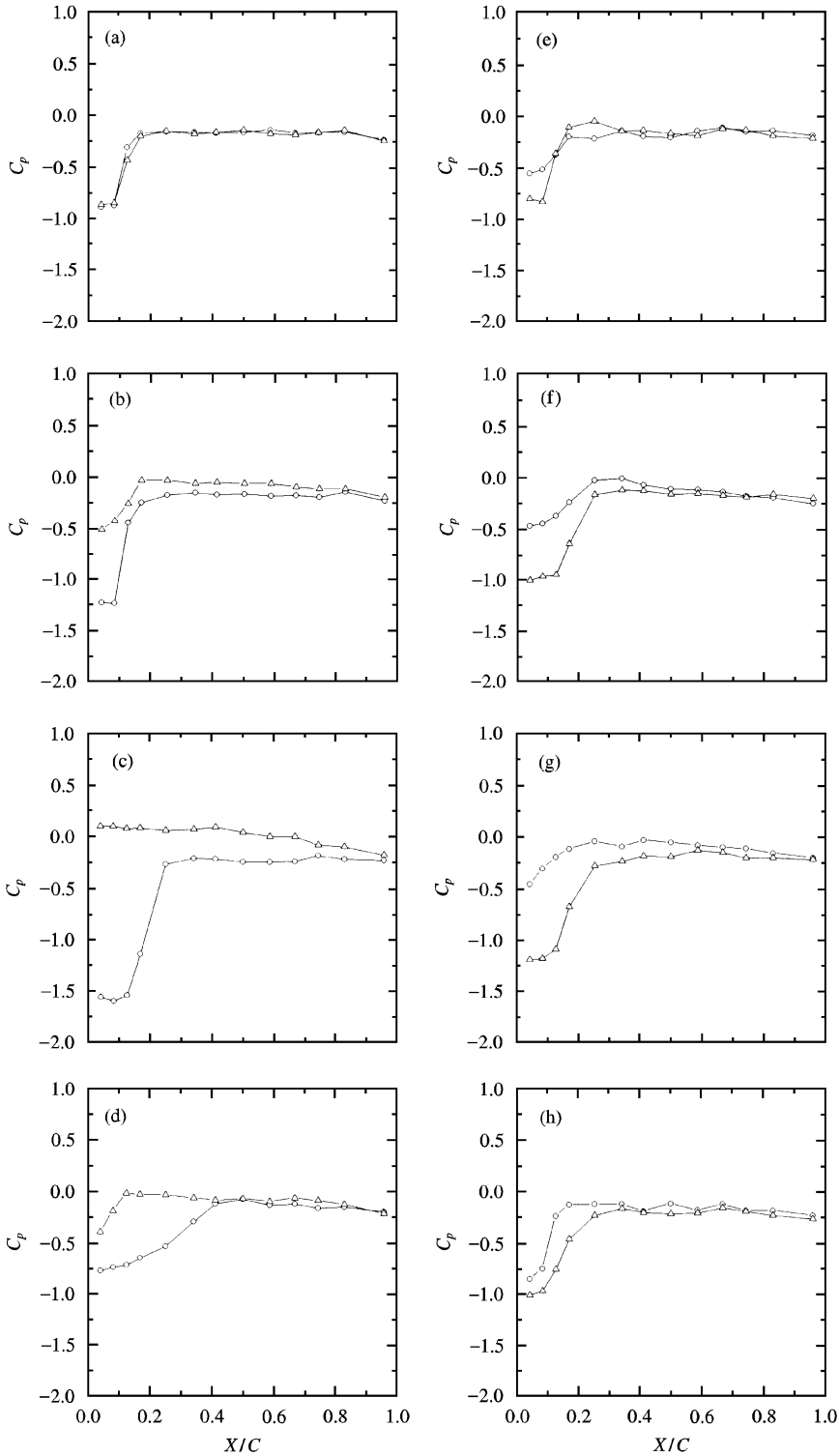

Figure 9. Pressure distributions on the square leading-edge plate at $Y_v/C = 0$ for various streamwise locations of the vortex; ○, upper surface; △, lower surface. (a) $X_vC = -1{\cdot}2$; (b) $X_v/C = -0{\cdot}5$; (c) $X_v/C = 0$; (d) $X_v/C = 0{\cdot}3$; (e) $X_v/C = 0{\cdot}6$; (f) $X_v/C = 1{\cdot}2$; (g) $X_v/C = 1{\cdot}7$; (h) $X_v/C = 2{\cdot}5$.

17–25% of the chord. Only for a short period (0·22–0·25 s), a disturbance of mild intensity on the pressure distribution extends further downstream. This may be due to the fact that the incident vortex is diffused and diminishes in strength when it passes over a distance downstream of the leading edge.

In order to reveal the details pertinent to the evolution of the surface pressure with respect to the incident vortex, the time axis of the measured pressure data is rescaled to the streamwise vortex location, with an assumption that the minimum value of the time history of pressure at the leading edge ($X/C = 0{\cdot}04$) occurs when the vortex center passes over it (Panaras 1987; Caradonna *et al.* 1988; Seath *et al.* 1989). The pressure port at $X/C = 0{\cdot}04$ was chosen because it had the most significant pressure pulse. It is further assumed that the vortex convects at a constant speed of 80% of the freestream velocity. The speed of convection is set at this constant value, $0{\cdot}80 \pm 0{\cdot}05\ U$, calculated from the pressure pulses and from the flow visualization. It should be noted that the exact vortex location, depending on the leading-edge shape and the vertical offset, may slightly differ from the point of the leading-edge minimum pressure (Kaykayoglu & Rockwell 1985). Nevertheless, the vortex location presented for the following pressure data has an accuracy (estimated in comparison with the flow visualization) of the order of the spatial resolution of the measuring pressure ports.

Figure 9 shows the pressure distributions at various streamwise locations of the vortex. At $X_v/C = -1{\cdot}2$, both distributions on the upper and lower surfaces nearly coincide, indicating no discernible effect of the incident vortex. It should be noted that due to the increase in the turbulence level the averaged reattachment point moves further forward than the case of quasi-steady flow (Kiya & Sasaki 1983*b*). At $X_v/C = -0{\cdot}5$, the vortex-induced upwash causes a decrease in pressure on the upper surface and an increase on the lower surface. As a result, a lift force acts on the plate. When the vortex collides with the plate leading edge, $X_v/C = 0$, the upper surface pressure reaches a minimum (maximum suction and lift). At the same time, on the lower surface the signal of leading-edge separation, i.e. a low-pressure region, disappears due to the strong vortex-induced upwash effect. As the vortex passes over the leading edge, at $X_v/C = 0{\cdot}3$, the upper surface pressure starts to rise while the lower surface pressure begins to descend, resulting in a decrease in lift. At $X_v/C = 0{\cdot}6$, the upper surface pressures near the leading edge turn to be higher than those on the lower surface, signifying a negative angle of attack. When the vortex moves to the trailing edge, the pressure distribution over the entire upper surface appears higher than that over the lower surface, meaning a negative lift. The area bounded by these two distributions continues to enlarge, until the vortex moves to $X_v/C = 1{\cdot}7$. Thereafter, a reduction in the bounded area is observed for $X_v/C = 2{\cdot}2$.

Figure 10 shows the surface pressure distributions at various streamwise locations of the incident vortex for the case of $Y_v/C = 0{\cdot}25$. Although the qualitative trend of the variations of pressure distribution at different vortex locations resembles that observed in the head-on interaction case ($Y_v/C = 0$), there are several differences between these two cases in quantitative details of the pressure distributions. As the incident vortex is located far upstream of the plate at $X_v/C = -1{\cdot}2$, the pressure distributions appear similar to those of the quasi-steady case (Figure 4), showing a region of low pressure followed by pressure recovery and then a higher level of pressure with a small negative gradient. This similarity is due to the fact that the passage of the smaller scale vortices above the plate have little effect on the separation bubbles along the plate and the downstream boundary layers as well. At $X_v/C = -0{\cdot}5$, a low-pressure region near the leading edge is retained on the lower surface, indicating that depression of the separation bubble caused by the vortex-induced upwash is

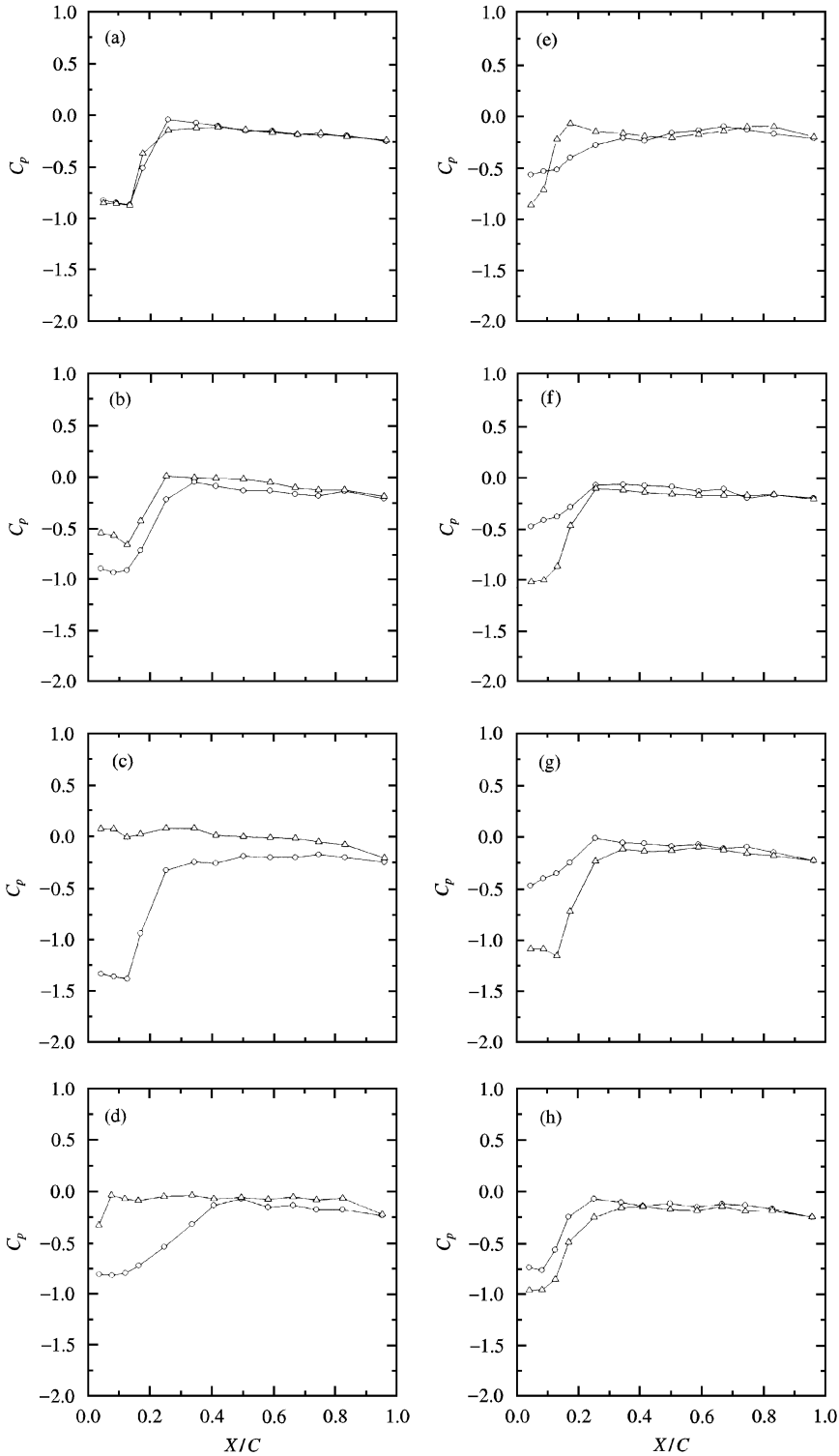

Figure 10. Pressure distributions on the square leading-edge plate at $Y_v/C = 0{\cdot}25$ for various streamwise locations of the vortex; ○, upper surface; △, lower surface. (a) $X_v/C = -1{\cdot}2$; (b) $X_v/C = -0{\cdot}5$; (c) $X_v/C = 0$; (d) $X_v/C = 0{\cdot}3$; (e) $X_v/C = 0{\cdot}6$; (f) $X_v/C = 1{\cdot}2$; (g) $X_v/C = 1{\cdot}7$; (h) $X_v/C = 2{\cdot}5$.

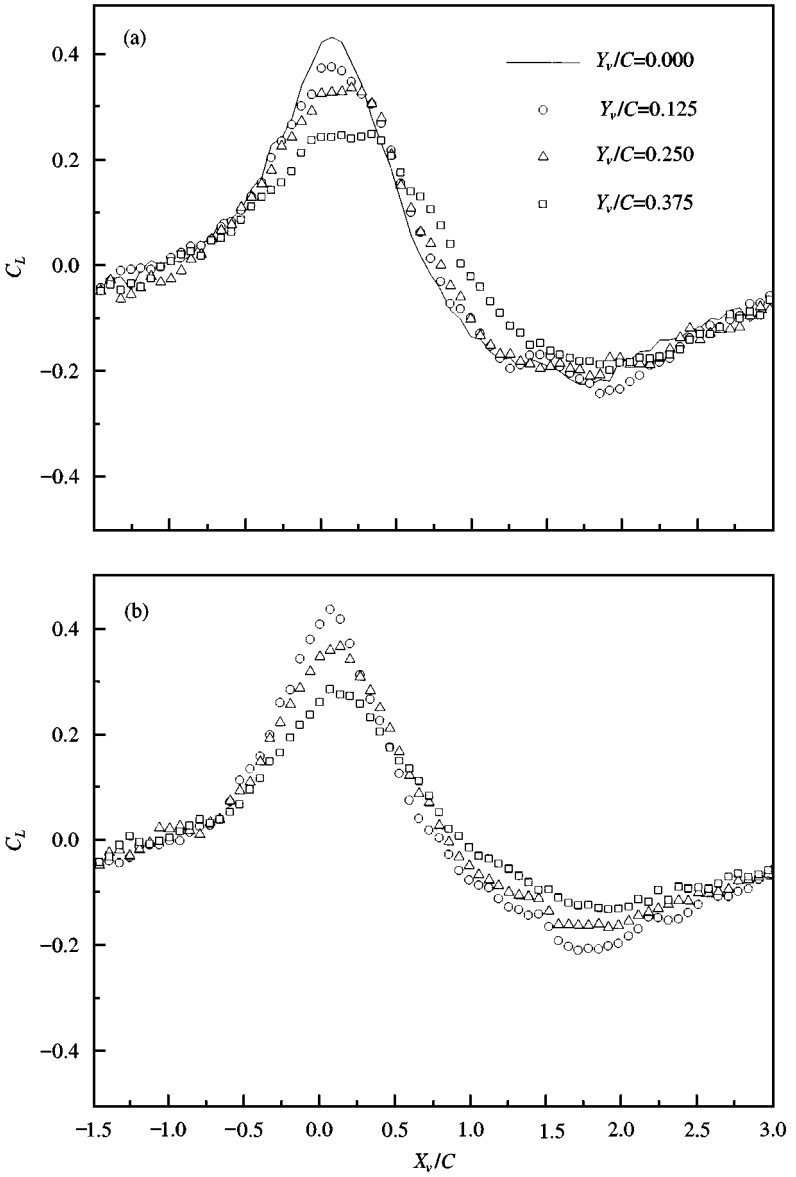

Figure 11. Variations of lift coefficient with the streamwise location of vortex for the square leading-edge plate at: (a) ——, $Y_v/C = 0$; ○, $Y_v/C = 0{\cdot}125$; △, $Y_v/C = 0{\cdot}25$; □, $Y_v/C = 0{\cdot}375$; (b) ○, $Y_v/C = -0{\cdot}125$; △, $Y_v/C = -0{\cdot}25$; □, $Y_v/C = -0{\cdot}375$.

less significant as compared with the case of $Y_v/C = 0$. The effect of adjusting the vertical offset to $Y_v/C = 0{\cdot}25$ is also apparent on the upper surface pressure distributions at $X_c/C = -0{\cdot}5$ and 0; the magnitude of the suction peak (minimum pressure) observed in Figure 10(b, c) is smaller than that which occurs in the case of $Y_v/C = 0$ by a value of about 0·25 in C_p. When the vortex passes over the plate leading edge, Figure 10(d–h) exhibits the change of the vortex-inudced upwash effect to downwash effect on the pressure distributions, reflecting the evolution of the separation bubble observed in Figure 7. Note that during the

post-interaction (vortex passing over the leading edge) period, the pressure distributions for the case of $Y_v/C = 0{\cdot}25$ are essentially identical to those for the case of $Y_c/C = 0$.

Surface pressure distributions are spatially integrated using an algorithm based on the trapezoidal rule to obtain lift coefficients. Figure 11 shows the variations of lift coefficient with the streamwise location of the incident vortex for different values of vertical offset. The uncertainty (due to random errors) of C_L presented is within 5% of the amplitude of lift coefficient variation. It is found that the lift begins to rise when the incident vortex approaches the plate leading edge near the $X_v/C = -0{\cdot}7$. The lift reaches a maximum as the vortex hits the leading edge. Then the lift decreases until the vortex moves to a chord length downstream of the plate trailing edge. The maximum and minimum values of the lift coefficient histories appear to be influenced by the vertical offset. The difference between the maximum and minimum lift coefficients (amplitude of lift coefficient variation), ΔC_L, decreases with the absolute value of vertical offset.

3.4. Effect of Leading-Edge Shape

Figure 12 shows the visualization of the head-on interaction of the incident vortex with the sharp leading-edge plate. It is observed in Figure 12(a) that, as the vortex approaches at about $X_v/C = -0{\cdot}6$, the plate experiences an increase in the angle of attack, leading to the formation of clockwise bound circulation in the vicinity of the leading edge. In response, the streaklines lying near the upper surface and immediately downstream of the leading edge are pulled towards the tip of the leading edge. As the vortex moves close to the leading edge, this clockwise bound circulation remains attached to the plate and continues growing until the incident vortex collides with the plate [Figure 12(b, c)]. The incident vortex is then split into two parts. When the split-incident vortex moves to the midchord of the plate [Figure 12(d)], the clockwise bound circulation can still be observed but is reduced in scale. Note that during the interaction, the separation bubble that appears in the cases of a square leading-edge plate is not observed.

The visualization of the interaction of the vortex with the sharp leading-edge plate at $Y_v/C = 0{\cdot}25$ is shown in Figure 13. Again, the approaching counter-clockwise vortex induces a clockwise bound circulation on the plate. Part of the clockwise circulation appears now in Figure 13 as a well-formed leading-edge separation vortex on the upper surface. This separation vortex is referred to as the secondary vortex by Swirydczuk *et al.* (1993) in their study of vortex–plate interaction. It is also observed that the vortex-induced upwash causes the stagnation point to shift from the tip of the sharp edge to a lower and slightly downstream position. For the interaction of the incident vortex with the elliptical leading-edge plate, the smoke visualization of the flow field is depicted in Figure 14. Formation of the secondary vortex and shift of the stagnation point is also visualized in this case.

Figures 15 and 16 demonstrate the pressure distributions on the sharp and elliptical leading-edge plates at $Y_c/C = 0{\cdot}25$, respectively. Both the cases of sharp and elliptical leading-edge plates have very similar pressure distributions. As the incident vortex reaches the leading edge, the vortex-induced upwash causes the upper surface pressure at the leading edge ($X/C = 0{\cdot}04$) to drop to a minimum value of about $-1{\cdot}4$ in C_p. The drop of the leading edge pressure is followed by a sharp rise of pressure in the forward 30% of the chord without forming a plateau of low pressure. Meanwhile, on the lower surface, a maximum pressure occurs at the leading edge, indicating a shift of the stagnation point to the lower surface. When the vortex convects to downstream of the trailing edge at

Figure 13. Smoke visualization of the interaction of the vortex with the sharp leading-edge plate at $Y_v/C = 0{\cdot}25$ and $X_v/C = -0{\cdot}15$.

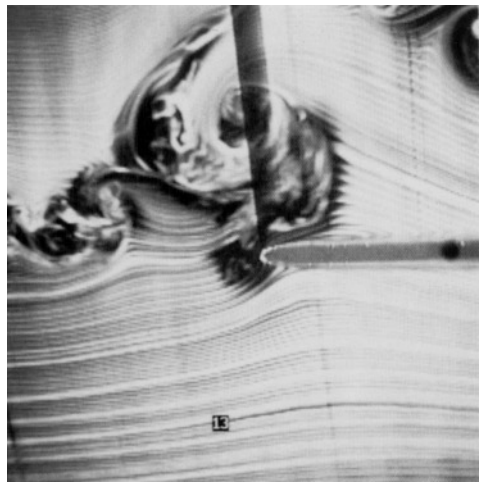

Figure 14. Smoke visualization of the interaction of the vortex with the elliptical leading-edge plate at $Y_v/C = 0{\cdot}25$ and $X_v/C = -0{\cdot}05$.

$X_v/C = 1{\cdot}7$, a downwash effect is observed in the figures, causing the pressure on the upper surface to be larger than that on the lower surface. The only discernible difference between the sharp and elliptical leading edges is the pressure at the leading edge ($X/C = 0{\cdot}04$). The pressure falls more rapidly on the sharp edge than on the elliptical edge, similar to what occurred in the quasi-steady flow case as shown in Figure 4.

The overall effects of the leading-edge shape and the vertical location of the incident vortex on the unsteady loading on the plate may be revealed by a plot of amplitude of lift coefficient variation ΔC_L versus dimensionless vertical offset Y_v/C, as presented in Figure 17 for the three types of plates. The amplitude of the lift coefficient decreases approximately linearly with vertical offset and seems to be independent of the sign of vertical offset,

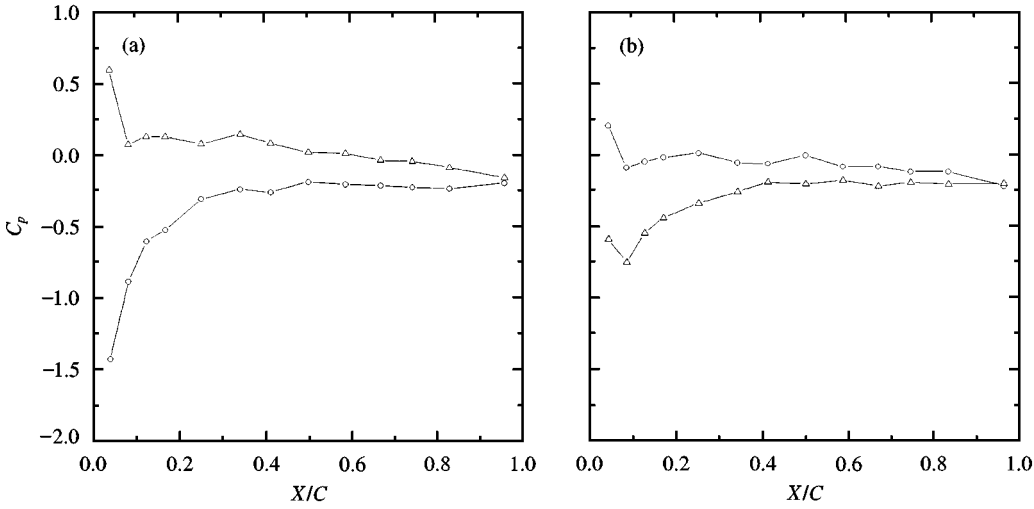

Figure 15. Pressure distributions on the sharp leading-edge plate at $Y_v/C = 0{\cdot}25$ for various streamwise locations of the vortex: ○, upper surface; △, lower surface. (a) $X_v/C = 0$; (b) $X_v/C = 1{\cdot}7$.

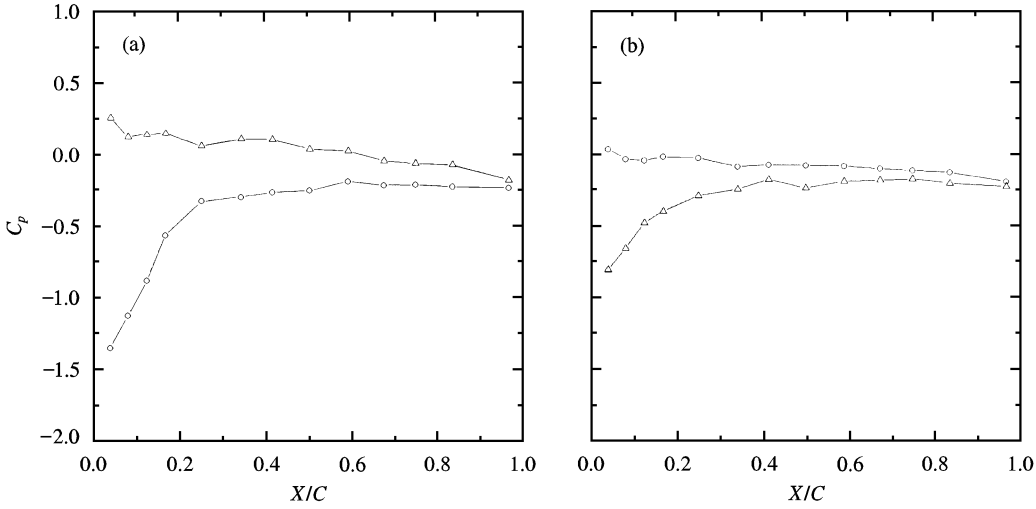

Figure 16. Pressure distributions on the elliptical leading-edge plate at $Y_v/C = 0{\cdot}25$ for various streamwise locations of the vortex: ○, upper surface; △, lower surface. (a) $X_v/C = 0$; (b) $X_v/C = 1{\cdot}7$.

indicating that the most severe interaction occurs for the head-on collision, i.e. $Y_v/C = 0$. The nature of the lift change in a similar manner for negative and positive offsets was also observed in the experiments of blade–vortex interaction by Horner *et al.* (1993). However, in an experimental study of vortex–wedge interaction by Ziada & Rockwell (1982), the amplitude of the induced lift was found to drop off more rapidly for negative values of offset than that for positive offsets (with the vortex orientation and the offset being redefined

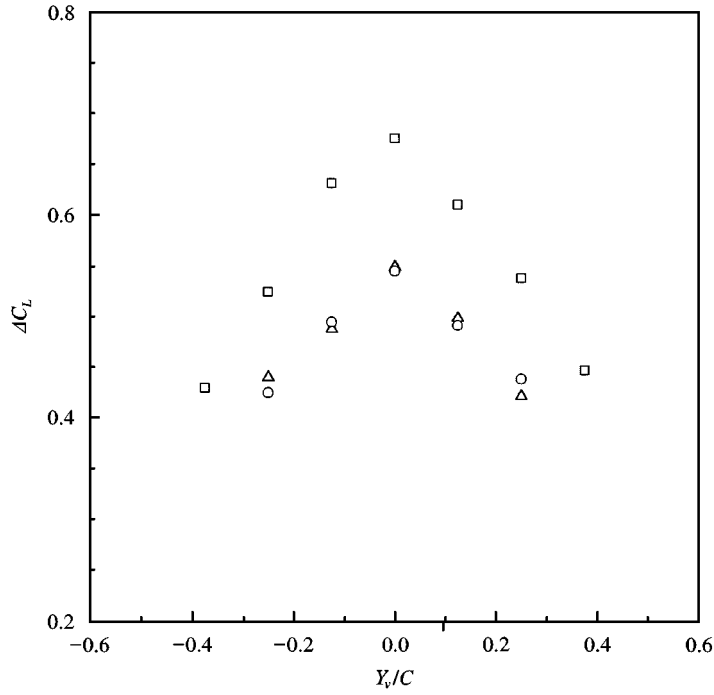

Figure 17. Amplitude of lift coefficient variation versus vertical offset of vortex generator for different plates: □, square leading edge; △, sharp leading edge; ○, elliptical leading edge.

consistently with the present study). This discrepancy may be partially due to the integration domain of surface pressure (Kaykayoglu & Rockwell 1985). For the present study, the lift force was determined from the integration of the pressure distribution over the entire surface of a long plate, rather than a small region in the neighborhood of the leading edge. Moreover, the relative scale and circulation of the incident vortical structure with respect to the plate geometry may have an effect, and this effect needs further study.

Figure 17 also displays that the amplitude of lift variation for the square leading-edge plate is larger than those for the sharp and elliptical plates by at least 25% at the same offset value. This difference is primarily due to the low pressure plateau region in response to the separation bubble formed along the square leading-edge plate. On the other hand, the results show that the geometric difference between the sharp and elliptical leading-edges has no discernible effect on the lift variation during the vortex–plate interaction. Apparently, the vortex-induced effects on the unsteady loading of a flat plate for initially separated flows are stronger than that for the initially attached flow. As far as the vortex-induced unsteady loading is concerned, it will be interesting to relate the amplitude of the lift coefficient variation ΔC_L to the corresponding change of strength of bound vortex induced around the plate in a uniform flow. This relation may be established by assuming steady flow during the occurrence of the extremum C_L. Therefore, according to the Kutta–Joukowski theorem for two-dimensional flow, the change of the bound vortex circulation $\Delta\Gamma_b$ is obtained by $\Delta\Gamma_b = 0{\cdot}5UC\Delta C_L$. It is found that for the sharp and elliptical leading-edge plates at $Y_v/C = 0$, their $\Delta\Gamma_b$ happens to be about twice the circulation of the incident vortex.

4. CONCLUSIONS

Flow visualization and surface pressure measurements were performed over long flat plates during interaction with an incident vortex in a wind tunnel. The incident vortex was produced by a vortex generator airfoil pitching in a tailored nonsinusoidal schedule. The interaction experiments were examined for plates having square, sharp and elliptical leading-edge shapes at a Reynolds number of 20 000 based on the plate chord length. The vertical offset of the vortex generator with respect to the plate was varied in the range $Y_v/C = -0{\cdot}375$ to $0{\cdot}375$. In all cases the results showed that an upwash effect starts to build up as the vortex approaches the plate at a distance of about 70% of a chord length upstream of the leading edge, causing a decrease in pressure on the upper surface and an increase on the lower surface. When the vortex arrives at the leading edge, the plate lift reaches its maximum. Subsequently, a downwash effect occurs as the vortex passes over the midchord of the plate, until the vortex convects to one chord length from the trailing edge.

The results of transient pressure distributions agree well with the observations of flow visualization. In comparison with the sharp and elliptical leading-edge plates, the amplitude of lift coefficient variation for the square leading-edge plate was found to be greater by at least 25%. This difference is primarily due to the low-pressure plateau region in response to the separation bubble formed along the square leading-edge plate. The separation bubble deforms significantly when the plate encounters the incident vortex. For the sharp and elliptical leading-edge plates, the only discernible effect caused by the difference in leading-edge shape appears on the pressure on the edge, but that has little influence on the amplitude of lift coefficient variation. It was also found that the amplitude of the lift variation decreases approximately linearly with the vertical offset of the incident vortex and is independent of the sign of the offset.

ACKNOWLEDGEMENTS

The authors gratefully acknowledge the financial support from the National Science Council of Taiwan, R.O.C. for this work through Grants NSC 85-2212-E-00-021 and NSC 86-2612-E-005-001.

References

Booth, E. R., Jr 1990 Experimental observation of two-dimensional blade-vortex interaction. *AIAA Journal* **28,** 1353–1359.

Caradonna, F. X., Lautenschlager, J. & Silva, M. 1988 An experimental study of rotor–vortex interactions. AIAA Paper 88-0045.

Chen, J. M. & Chang, D.-M. 1997 Unsteady pressure measurements for parallel vortex-airfoil interaction at low speed. *Journal of Aircraft* **34,** 330–336.

Chen, J. M. & Shieh, Y.-T. 1997 Flow visualization of parallel vortex–airfoil interaction. *Proceedings of the 1st Pacific Symposium on Flow Visualization and Image Processing*, Honolulu, Hawaii, pp. 120–125.

Cherry, N. J., Hillier, R. & Latour, M. E. M. P. 1984 Unsteady measurements in a separated and reattaching flow. *Journal of Fluid Mechanics* **144,** 13–46.

Horner, M. B., Saliveros, E., Kokkalis, A. & Galbraith, R. A. McD. 1993 Results from a set of low speed blade–vortex interaction experiments. *Experiments in Fluids* **14,** 341–352.

Kaya, M. O. & Kaykayoğlu, C. R. 1996 Numerical simulation of a self-sustained wake–edge interaction. *Journal of Fluids and Structures* **10,** 215–236.

KAYKAYOGLU, C. R. & ROCKWELL, D. 1985 Vortices incident upon a leading edge: instantaneous pressure fields. *Journal of Fluid Mechanics* **156,** 439–461.
KIYA, M. & SASAKI, K. 1983*a* Structure of a turbulent separation bubble. *Journal of Fluid Mechanics* **137,** 83–113.
KIYA, M. & SASAKI, K. 1983*b* Free-stream turbulence effects on a separation bubble. *Journal of Wind Engineering and Industrial Aerodynamics* **14,** 375–386.
LUGT, H. T. 1983 *Vortex Flow in Nature and Technology*, pp. 28–34, New York: Wiley.
MOOK, D. T. & DONG, B. 1994 Perspective: numerical simulation of wakes and blade–vortex interaction. *ASME Journal of Fluids Engineering* **116,** 5–21.
OTA, T. & ITASAKA, M. 1976 Separated and reattached flow on a blunt flat plate. *ASME Journal of Fluids Engineering* **98,** 79–86.
PANARAS, A. G. 1987 Numerical modeling of the vortex/airfoil interaction. *AIAA Journal* **25,** 5–11.
PARK, J.-H. & LEE, D.-J. 1994 Numerical simulation of vortex–wedge interaction. *AIAA Journal* **32,** 1126–1134.
SEATH, D. D., KIM, J.-M. & WILSON, D. R. 1989 Investigation of the parallel blade–vortex interaction at low speed. *Journal of Aircraft* **26,** 328–333.
STRAUS, J., RENZONI, P. & MAYLE, R. E. 1990 Airfoil pressure measurements during a blade–vortex interaction and a comparison with theory. *AIAA Journal* **28,** 222–228.
SWIRYDCZUK, J. 1990 A visualization study of the interaction of a free vortex with the wake behind an airfoil. *Experiments in Fluids* **9,** 181–190.
SWIRYDCZUK, J., WILDER, M. C. & TELIONIS, D. P. 1993 The interaction of coherent vortices with short flat plate. *ASME Journal of Fluids Engineering* **115,** 590–596.
ZIADA, S. & ROCKWELL, D. 1982 Vortex-leading-edge interaction. *Journal of Fluid Mechanics* **118,** 79–107.

APPENDIX: NOMENCLATURE

C	chord length of flat plate
C_L	lift coefficient $[L/(\rho U^2 C/2)]$
ΔC_L	amplitude of lift coefficient variation
C_p	pressure coefficient $[(p - p_\infty)/\frac{1}{2}\rho U^2)]$
H	plate thickness
L	lift force/length
p	pressure
p_∞	freestream static pressure
Re	Reynolds number, UC/ν
U	freestream velocity
X	streamwise distance from plate leading edge
X_v	streamwise location of incident vortex with respect to plate leading edge
Y	vertical distance from plate centerline
Y_v	vertical offset of vortex generator with respect to plate
Γ	vortex circulation
$\Delta\Gamma_b$	change of bound vortex circulation
ρ	fluid density
ν	kinematic viscosity

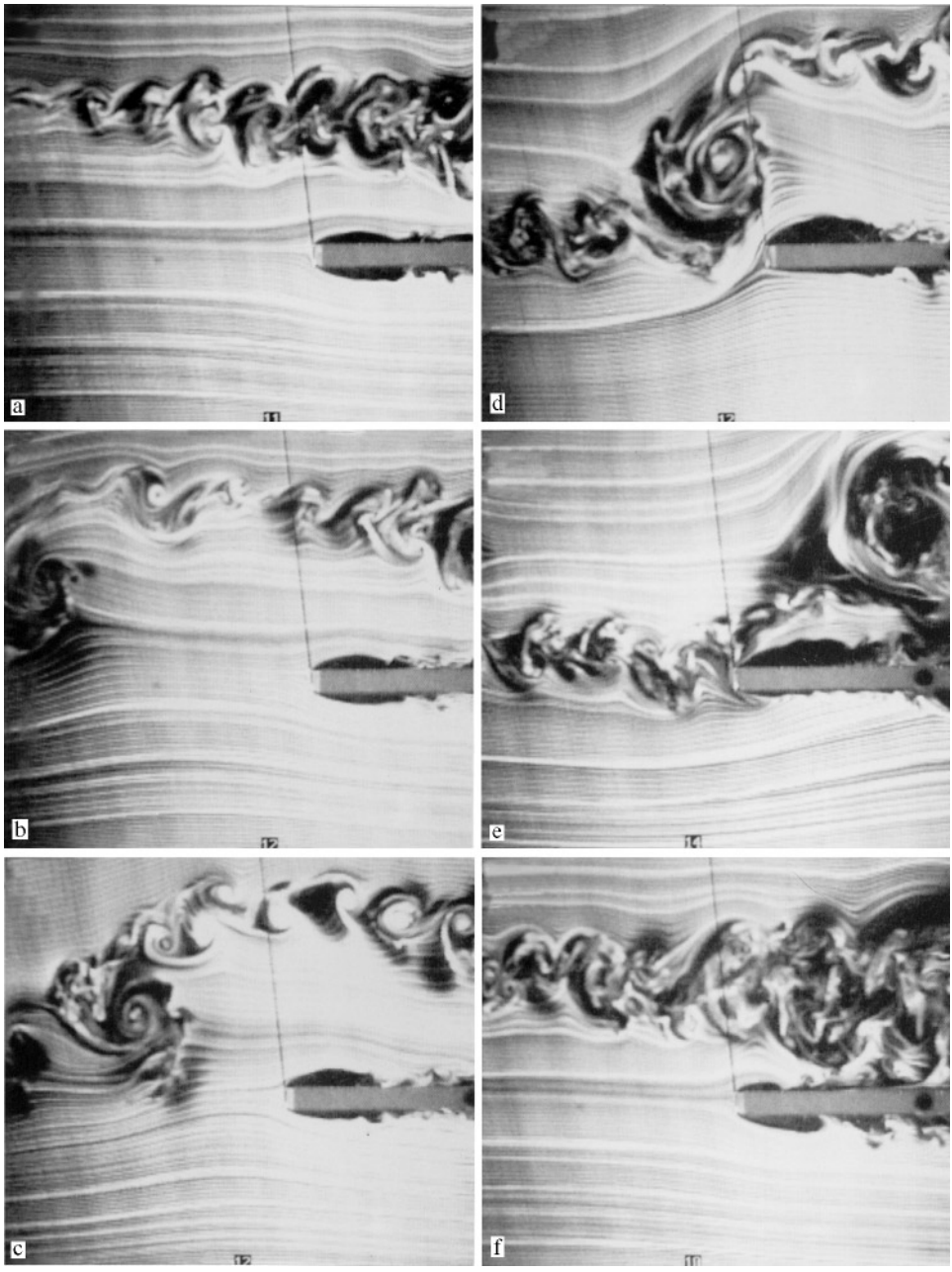

Figure 7. Smoke visualization of the interaction of the vortex with the square leading-edge plate at $Y_v/C = 0{\cdot}25$. Time intervals relative to (a) are: (b) 0·037 s; (c) 0·050 s; (d) 0·066 s; (e) 0·100 s; (f) 0·150 s.

Figure 12. Smoke visualization of the interaction of the vortex with the sharp leading-edge plate at $Y_c/C = 0$. (a) $X_v/C = -0{\cdot}6$; (b) $X_v/C = -0{\cdot}1$; (c) $X_v/C = 0$; (d) $X_v/C = 0{\cdot}5$.